Study on Hydration and Dehydration of Ezetimibe by Terahertz Spectroscopy with Humidity-Controlled Measurements and Theoretical Analysis

Mizuki Mohara,* Margaret P. Davis, Timothy M. Korter, Kei Shimura, Touya Ono, and Kenji Aiko

Read Online

ACCESS | Metrics & More | Article Recommendations | SI Supporting Information

ABSTRACT: Understanding the solid-state transitions of active pharmaceutical ingredients (APIs) is essential for quality control since differences in their forms affect the bioavailability of APIs. Terahertz (THz) frequency-domain spectroscopy is suitable for such an application since it can sensitively probe the lattice phonon modes originating in the crystal structures. THz absorption spectra were obtained for ezetimibe (EZT) and ezetimibe monohydrate (EZT-MH), which have similar crystalline structures and belong to the same space group. The observed absorption spectrum of EZT matched well with the solid-state density functional theory (ss-DFT)-simulated spectrum for the structures at 0 K and room temperature (modeled using constrained unit cell volumes). However for EZT-MH, the ss-DFT spectrum of the room-temperature structure showed better correlation with the experimental THz spectrum than that of the simulated spectrum of the 0 K structures, suggesting that the EZT-MH crystal has greater anharmonic character. Gibbs free-energy curves were calculated, and EZT-MH was found to be more stable than pure EZT and water in a broad temperature range. The hydrate stability may be influenced by the existence of more hydrogen bonds in EZT-MH. The hydration and dehydration of EZT in a pure API tablet and formulation tablets were monitored using a THz spectrometer with a humidity-controlled sample chamber. The effect of the excipient in the formulation tablet on hydration was successfully confirmed by showing that the solid-state transition of the API with excipients is significantly slower than that without it. Under a relative humidity of 60%, hydration of EZT in a pure EZT tablet occurred in 200 min, while the hydration of EZT in a formulation tablet was 50 times slower.
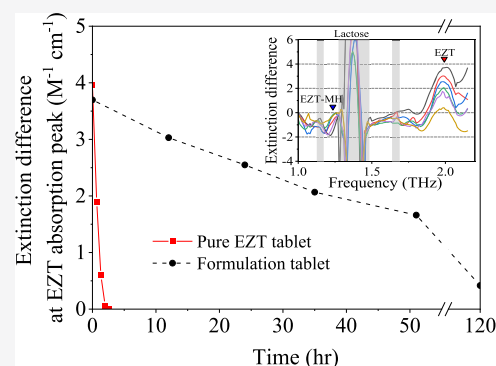
■ INTRODUCTION

Analyzing crystalline forms, such as polymorph and hydrate/anhydrous forms, of active pharmaceutical ingredients (APIs) in formulation tablets is essential for quality control of pharmaceutical tablets. Different crystalline forms of an API can produce different properties, such as altered solubility, melting point, and density.[1] Transition between crystalline forms during pharmaceutical manufacturing processes such as mixing, granulation, drying, and tableting processes have been reported.[2] In addition, unstable and metastable forms could be transformed to a stable form under standard storage conditions. Therefore, identifying a stable form of an API and confirming it in formulation tablets and after production processes are necessary for ensuring quality of pharmaceutical products.[3]

Approximately one-third of pharmaceutical molecules are thought to be capable of forming crystalline hydrates.[4] Hydrates usually have lower dissolution rates than anhydrates,[5] and pharmaceutical excipients affect hydration and dehydration reactions in formulations that contains API and some excipients.[6] However, very few spectroscopic studies on the crystalline form in pharmaceutical formulations have been

reported because of the difficulties of understanding the complex spectra resulting from multiple compounds. Also, monitoring and understanding the hydration and dehydration reactions of APIs in formulations are important for pharmaceutical manufacturers to select suitable excipients. Crystal structures of hydrates transform upon dehydration since removal of water induces the change in the internal structure, and some hydrates also become amorphous when dehydrated.[7] Others retain their three-dimensional packing arrangements with hydration and dehydration transitions.[7] For example, erythromycin A is a widely used macrolide antibiotic and is known for having structural similarity between its dihydrate and anhydrate forms, and similar powder X-ray diffraction (PXRD) patterns between the hydrate and anhydrate forms are observed.[6,8]
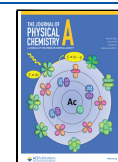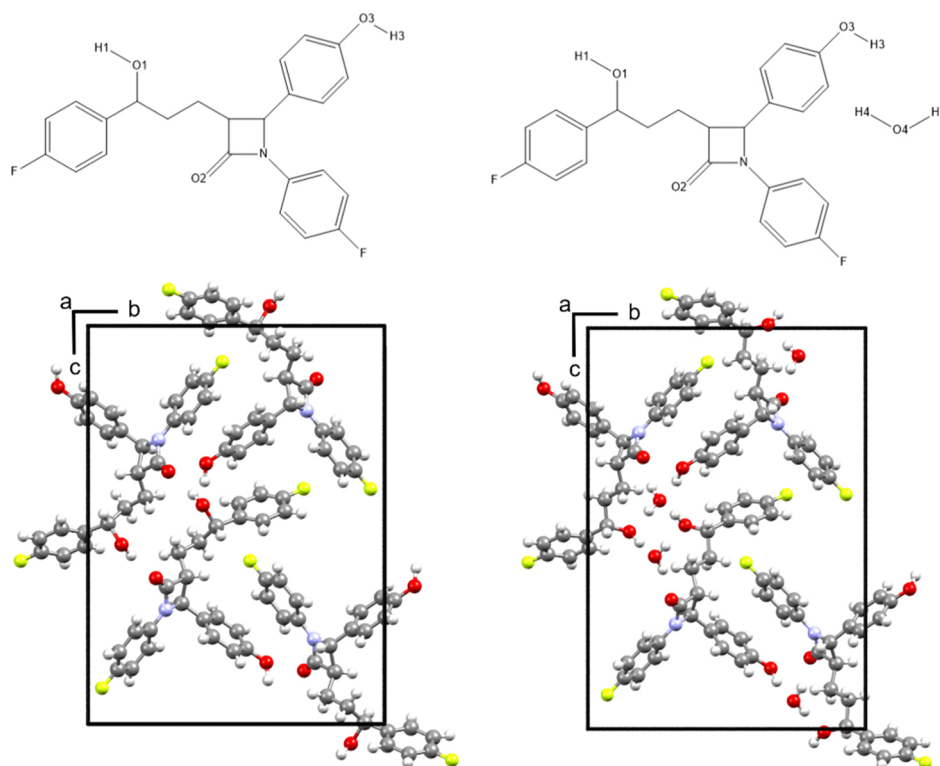
Figure 1. EZT (top, left), EZT-MH (right, top), and crystallographic unit cells for EZT (bottom, left) and EZT-MH (bottom, right). Only atoms involved in hydrogen bonding are labeled in the two-dimensional representations.

PXRD is widely used to identify crystalline forms in the pharmaceutical field and determine crystal structures directly. The combination of PXRD and calorimetric techniques such as differential scanning calorimetry and thermogravimetric analyses are powerful tools for evaluating the formation of hydrates and dehydrates of APIs.[6,8,9] Mid- and low-frequency Raman spectroscopy is sensitive to the solid-state structure and applied to identify hydrates.[10,11] Since terahertz (THz) radiation is located at the far-infrared region, THz spectroscopy can directly probe the lattice phonon modes originating from the crystal structure contents and specific packing. Using THz time-domain spectroscopy (THz-TDS), the identification of hydrates and anhydrates has been reported.[12−14] Also, novel solid-state density functional theory (ss-DFT) calculations for hydrate and anhydrate organic crystals have been performed to assign the vibrational modes of their THz absorption spectra.[12,15]

An injection-seeded THz parametric generation (is-TPG) technique has been developed for realizing a high-peak-power THz wave source,[16] and it has been used for THz frequency-domain spectroscopy (THz-FDS).[17−19] Although THz-TDS generally has a high dynamic range below 1 THz, an is-TPG source has the highest dynamic range between 1.5 and 2.0 THz,[17] where a number of characteristic absorption peaks exist. Its high-peak-power THz wave and large dynamic range over a wide frequency range make it applicable to inspecting crystal structures in a formulation tablet without sample damage. The transmission THz spectrometer with an intense THz source such as this makes it possible to inspect a whole sample tablet,[19] not only the surface of the sample or a small portion of the sample like in other microscopic methods. Thus, it has another advantage, the ability to detect changes in crystalline forms directly in a formulation tablet.

In this work, we theoretically analyze the crystal structures and THz absorption spectra of ezetimibe anhydrous (EZT) and ezetimibe monohydrate (EZT-MH) and identify the solid-state transition between the two using THz-FDS with an is-TPG technique. EZT is used for cholesterol and lipid reduction in blood and is considered as Class II in the Biopharmaceutical Classification System, which means the API has low solubility in water but high permeability.[20,21] EZT exists in the solid state in both anhydrous[22] and monohydrate[23] forms with very similar crystalline morphologies, with both belonging to the same $P2_12_12_1$ space group (Figure 1). Although several pieces of research on improving the solubility of EZT have been reported, studies in the literature about different crystalline forms of EZT are limited.[21,24,25] Here, we have demonstrated monitoring of the hydration and dehydration of ezetimibe in real time using THz-FDS with the is-TPG source and a humidity-controlled sample chamber and verified the effect of excipients in the pharmaceutical formulation on the solid-state phase transformation. Additionally, ss-DFT calculations were used to simulate the crystal structures and vibrations of EZT and EZT-MH to assign the THz spectra. In order to understand the stability of EZT-MH, the Gibbs free-energy curves for EZT-MH and EZT were calculated using ss-DFT to better define the temperature dependence of the different forms.

■ METHODS

Materials. EZT was purchased from Toronto Research Chemicals. EZT-MH was obtained by keeping EZT at room temperature at a relative humidity (RH) of 55−75% overnight.[21] The EZT-MH form was confirmed by PXRD (Rigaku, MiniFlex600), as shown in the Supporting Information. The PXRD peaks at 7.82 and 24.46° matched

Table 1. Compositions of Sample Tablets (wt %)

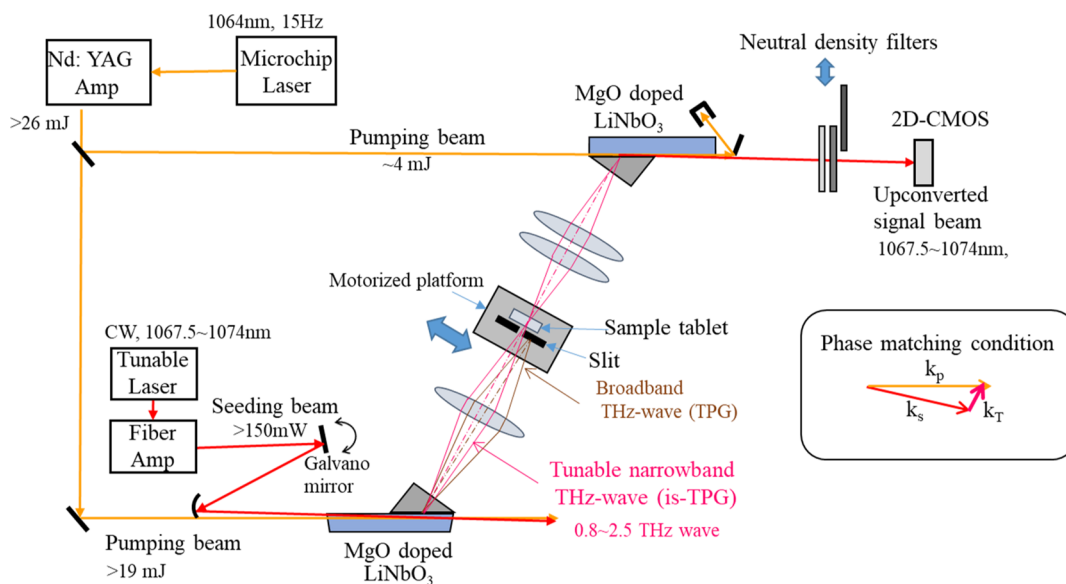| tablet name | ezetimibe | | polyethylene | lactose monohydrate | crystalline cellulose | thickness (mm) | weight (mg) |
	anhydrate	monohydrate					
pure EZM	80		20			1.3	109
pure EZT-MH		80	20			2.5	197
formulation	10			45	45	1.9	226
placebo				50	50	1.9	226

Figure 2. Schematic of the FD-THz spectrometer with is-TPG. Slit for eliminating TPG waves is placed in front of the sample and moved depending of the wavelength of the is-TPG. Footprint is 0.7 m².

with those of previous study about EZT-MH.[21] The sample powders were weighed and mixed, as shown in Table 1, and pressed into 10 mm diameter tablets at a pressure of 4.9 kN in 10 s for the measurement of the THz absorption spectra of pure EZT and EZT-MH. Ultra-high-molecular-weight polyethylene (Sigma-Aldrich) was used as the diluent. Since the THz-wave absorption of EZT-MH is low, the tablet thickness was about twice that of EZT. To measure the hydration and dehydration of a pharmaceutical formulation tablet, a sample tablet was used that contained 10% EZT as an API and lactose monohydrate (Wako Pure Chemical Corporation, guaranteed reagent) and crystalline cellulose (Asahi Kasei Corporation, ST-100, particle size: 50 μm) as additives. A placebo (no API) tablet was prepared to compare the absorption spectra of the formulation tablet and the placebo tablet. The sample powder of the formulation and placebo tablets were pressed into 10 mm diameter tablets at a pressure of 49 kN in 2 min. The high pressure was needed to avoid the disintegration of the sample tablets due to the absorption of humidity by additives. The thickness of the pure EZT tablets normalized by its weight was thicker than that of the formulation tablets. This may come from the differences in density between EZT and the additives.

Terahertz Spectrometer. Figure 2 shows the developed frequency-domain THz (FD-THz) spectrometer with is-TPG.[19] Light emitted from a Q-switched Nd:YAG microchip laser (L11038-11, Hamamatsu Photonics) at a 15 Hz repetition rate (wavelength: 1064 nm) was amplified up to 26 mJ by double-pass Nd:YAG amplifiers (POD-CS3/300P-NY3, PHLUXi). This amplified high-peak-power light was focused on a MgO-doped LiNbO3 (LN) crystal and used as a pump light for generating is-TPG waves. The output light of a

continuous-wave (CW) tunable diode laser with a single longitudinal mode (TLB6722-P, Newport) was also amplified up to 150 mW by a fiber amplifier (CTFA-PB, Keopsys). This amplified CW beam was introduced into the LN crystal as a seed light to generate is-TPG waves parametrically. The relationship among the pump light, seed light, and generated is-TPG waves satisfies the non-collinear phase-matching condition, as shown in the inset of Figure 2. The is-TPG waves from 0.8 to 2.5 THz were generated by scanning the wavelength of the seeder laser from 1067.5 to 1074 nm. The angle of the seeding beam to the pumping beam was adjusted with high accuracy using a galvano mirror for every wavelength during the scanning. The relationship between the surface of the crystal and the galvano mirror was designed to be optically conjugate using a concave mirror in order to make the beam position of the seed light stay on the surface of the crystal at the same position when the angle of the seeding beam was changed using the galvano mirror for a selected wavelength. The surface of the LN crystal was cut off at an angle of 4° to avoid optically damaging the seed optical system using the pump light reflected at the front surface of the crystal. Adopting the galvano mirror makes it possible to establish a compact and practical seed optical system. A Si prism placed on the side of the LN crystal was used as an efficient output coupler for the THz waves. A slit mounted on a linear stage was inserted in the THz optics between the LN crystal and a sample to effectively expand the spectral range of the spectrometer.

When an is-TPG wave was generated at the first LN crystal, a weak and broadband unseeded TPG wave was simultaneously generated by the intense pulsed pump beam without

the effect of the seeding beam. This broadband TPG wave was generated preferentially in a region of the seeded frequency but less than 1.2 THz and higher than 2.5 THz, where the is-TPG conversion efficiency was low. The intensity of this TPG wave was unstable and affected the dispersion of the signal intensity of the spectra. To eliminate this TPG wave with an emission angle different from that of the is-TPG wave, the generated THz waves were focused on the slit, and the position of the slit was adjusted by a linear stage so that the is-TPG wave passed through the slit, and the TPG wave was blocked. Using this configuration in the frequency region with a lower conversion efficiency for is-TPG waves, and even if the is-TPG light transmitted through the sample tablet was weak, the signal light could be detected.

Generated high-purity is-TPG waves were focused on a sample tablet that was mounted on a holder in a humidity-controlled chamber. The RH in the chamber was controlled to lower than 1% for dry measurements and approximately 60% for non-dry measurements. Mixing the THz waves transmitted through the sample tablet with the pump light in another MgO-doped $LiNbO_3$ crystal generated an upconverted signal. The upconverted signal light was attenuated by multiple neutral density (ND) filters after being separated from the pump light and was detected by a 2D-CMOS camera in synchronization with the emission of the pump light. All absorption spectra in this work were smoothed using a Savitzky−Golay filtering method. In the case of non-dry measurements, the absorption peaks of water vapor in the measured data were removed by preprocessing the spectra. The frequency calibration of the absorption spectra measured with this THz spectrometer was accomplished using the known frequencies of the absorption peaks of water vapor (Figure 2).[26,27]

Theoretical Analysis. CRYSTAL17[28] was used to complete ss-DFT simulations of EZT and EZT-MH including geometry optimizations, frequency simulations and assignments, and energetic analyses. For all of the calculations, Ahlrichs' VTZ basis set with additional polarization functions[29] was used with the Perdew−Burke−Ernzerhof[30] density functional. Grimme's London dispersion correction[31−33] (D3) utilizing the Becke−Johnson damping correction and three-body Axilrod−Teller−Muto repulsion contributions[34] (program keyword "ABC") were included. For EZT and EZT-MH, the number of k-points in the irreducible Brillouin zone was set to 125 (program keyword SHRINK 8 8). For all calculations with both systems, the overlap-based truncation criteria for the bielectronic integrals (Coulombic and exchange, program keyword TOLINTEG) were set to 10^{-10}, 10^{-10}, 10^{-10}, 10^{-10}, and 10^{-20}.

The crystal structure of EZT has been deduced from using PXRD methods, while single-crystal X-ray diffraction measurements have been reported for EZT-MH. There is a published single-crystal structure for EZT; however, it is a different chirality (R, S, R instead of the correct S, R, S) from the clinically administered form used in this work.[25] The starting structures for EZT and EZT-MH geometry optimizations were obtained from the Cambridge Structural Database[35] (CSD) with reference codes QUWYIR[22] and QATNEF01,[23] respectively. The energy convergence criteria for geometry optimizations were set to $\Delta E < 10^{-8}$ hartree. Two types of geometry optimizations were performed. First, geometry optimizations were performed where the lattice parameters and the atomic positions were allowed to freely optimize (the

only constraint being the crystal space group), with results referred to as the "fully optimized" structure and representative of the structures at 0 K. Second, geometry optimizations were performed where only the atomic positions were allowed to optimize, and the lattice parameters were held constant to their experimental values, referred to here as the "fixed-lattice" structure (program keyword ATOMONLY). Since both previously reported experimental structures were solved at room temperature (293 K, unit cell volume = 2019.688 Å^3 for EZT[22] and 296 K, unit cell volume = 2161.395 Å^3 for EZT-MH[23]), the fixed-lattice calculations were an approximation used to better simulate the properties of the room-temperature samples studied in this work. Frequency analyses were performed on both the fully optimized and fixed-lattice structures of EZT and EZT-MH with energy convergence criteria of $\Delta E < 10^{-10}$ hartree. The central difference formula was employed to calculate the numerical derivative of the Hessian matrix with each atom having two displacements along each Cartesian axis. Infrared spectral intensities were calculated using the Berry phase method.[36,37]

CRYSTAL17 was also used to perform energy analyses on the EZT and EZT-MH crystals (both fully optimized and fixed-lattice structures). Conformational energies of ezetimibe were calculated by performing a single-point molecular energy calculation on an isolated molecule extracted from each periodic system. For the EZT crystal, cohesive energies were calculated by subtracting the conformational energy of the isolated ezetimibe molecule from the total electronic energy of the solid. In the EZT-MH, the conformational energies of both the isolated ezetimibe and water molecules were subtracted from the total electronic energy of the hydrated crystal. The final aspect of energy analysis was the construction of Gibbs free-energy curves from 0 to 700 K for the ezetimibe samples using both the fully optimized and fixed-lattice simulated structures and vibrational frequencies.

■ RESULTS AND DISCUSSION

Experimental Terahertz Vibrational Spectra. Figure 3 shows the THz frequency-domain absorption spectra of the pure EZT and EZT-MH tablets. Extinction was calculated for the vertical axis on the basis of the concentration of the sample and the thickness of the tablets and represents both the absorption and scattering of THz waves in the tablets. The
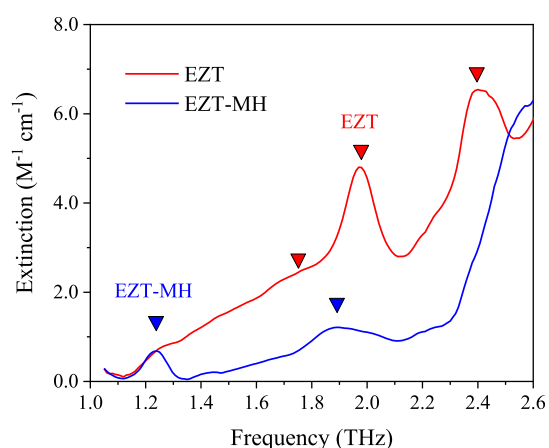

Figure 3. FD-THz absorption spectra of pure EZT (thickness = 1.3 mm) and EZT-MH (thickness = 2.5 mm) tablets.

base line of these spectra gradually increased in the high-frequency region, most likely because of Mie scattering inside the tablets. Main cause of the scattering was assumed to be difference in the refractive index between EZT and EZT-MH since the particle size of EZT-MH, which is prepared from the EZT powder, is expected to be the same as that of the EZT sample. Absorption peaks of EZT appeared at 1.75, 1.98, and 2.42 THz, and those of EZT-MH appeared at 1.24 and 1.88 THz. Anhydrate and hydrate were clearly identified on the basis of the differences in these characteristic absorption peak positions, which corresponded to the difference in vibrational modes between the crystal structures.

Absorption spectra of a pure EZT-MH tablet were repeatedly measured while keeping the tablet in a dry condition (Figure 4a). The absorption peaks of EZT-MH at
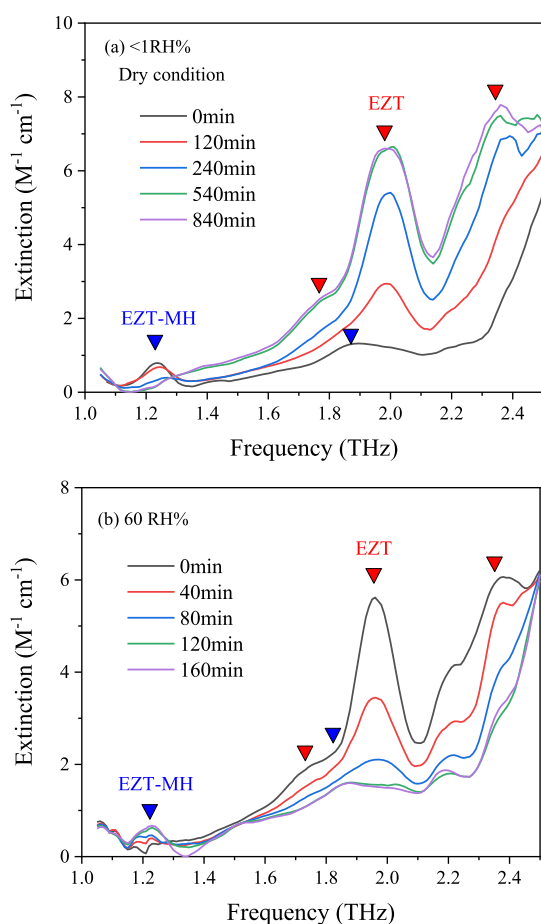

Figure 4. Absorption spectra of ezetimibe tablet (thickness = 2.5 mm) kept in a sample chamber at (a) <1 RH % and (b) 60 RH %.

1.24 and 1.88 THz decreased gradually, and those of EZT at 1.75, 1.98, and 2.42 THz increased. EZT-MH completely dehydrated after 900 min. On the other hand, keeping the EZT tablet at RH 25%, the absorption peaks of EZT decreased, and those of EZT-MH increased, which means that the hydration of EZT was observed (Figure 4b) over a span of 200 min. Under non-dry measurement conditions, strong narrow absorption peaks of water vapor appeared. These peaks could be removed, and the data interpolated linearly since the widths of the absorption peaks of water vapor were much narrower than those of EZT and EZT-HM.

Figure 5a shows the absorption spectra of the formulation and placebo tablets under dry conditions. Before starting the
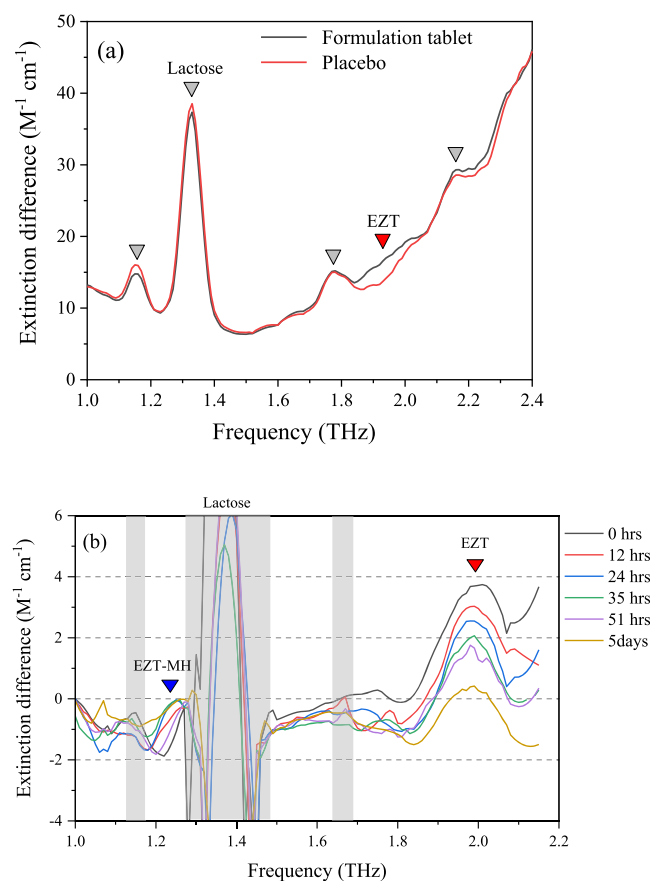

Figure 5. Observation of hydration of ezetimibe in a formulation tablet; (a) THz absorption spectra of the formulation and placebo tablets measured under dry conditions and (b) their difference from spectra of the placebo tablet which were repeatedly measured at a RH of approximately 60%.

measurement, the tablet containing the ezetimibe was kept at a RH of <1% overnight, which means that all the ezetimibe in the tablet was initially in the anhydrate form. There was an extinction difference around 1.98 THz of the spectra of the EZT tablet and the placebo tablet, corresponding to the absorption peak of EZT. Strong absorption peaks of lactose at 1.20, 1.38, 1.82, and 2.20 THz appeared in both spectra. In the high-frequency region, the extinction became large due to the absorption and scattering of cellulose in the tablets. Absorption spectra were repeatedly measured at room temperature and at a RH of approximately 60%. To make the change in the absorption peaks of EZT more apparent, interference from the strong absorption peaks of lactose was reduced by subtracting the placebo's spectrum from the spectra of the formulation tablet, as shown in Figure 5b. The extinction changes at 1.98 THz, corresponding to the absorption peak of EZT, showed a positive peak at 0 min but decreased over time. After 5 days, hydration of EZT was completed. In comparison with the hydration of the pure EZT tablet, the formulation tablet hydration rate was less than one-fiftieth of that of the pure EZT tablet due to the presence of the lactose and cellulose excipients, as shown in Figure 6. Using our FD-THz spectrometer with the humidity-controlled measurement chamber, the hydration and dehydration processes of APIs in
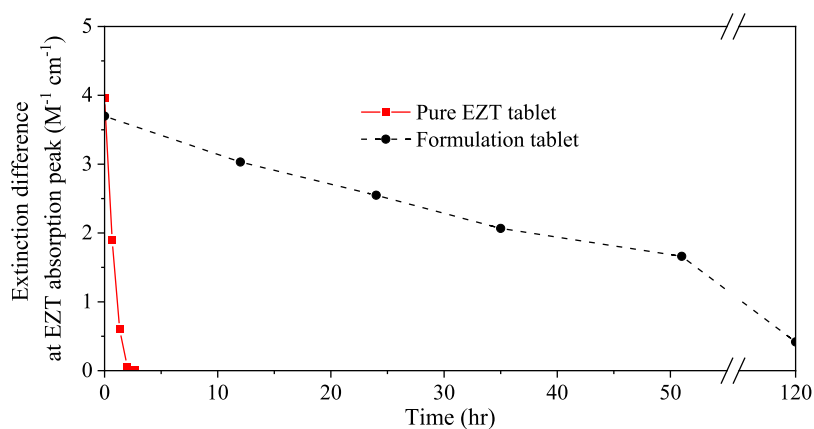
Figure 6. Time-dependent extinction changes at 1.98 THz, corresponding to an EZT absorption peak, in a non-dry environment (60% RH). Hydration of EZT in both pure and formulation tablets was observed.

formulation tablets could be monitored successfully including tablets with and without excipients.

Polymorph Differences and Optimized Structures. *Evaluation of the ss-DFT-Optimized Structures.* The accuracy of the optimized crystal structures is paramount when simulating low-frequency vibrational spectra and evaluating energy factors in the solids. The ss-DFT fully optimized structures of EZT and EZT-MH matched well with the experimental data, as summarized in Table 2. The highest

Table 2. Unit Cell Dimensions (Å) of EZT from the Experiment (CSD Structure QUWYIR[22]), after Ss-DFT Optimization, and the Percent Error between the Two

lattice parameter	experimental	calculated	percent error (%)
a	5.94606	5.900256	−0.77
b	15.8898	15.91676	0.17
c	21.3765	21.17691	−0.93
volume (Å³)	2019.6882	1988.78539	−1.53

percent error in the fully optimized EZT unit cell dimensions was −0.93% on the *c*-axis, with the average absolute error in the calculated unit cell dimensions being 0.62%. Although the lattice parameters were compared to the powder X-ray structure, the internal structure was compared to single-crystal X-ray structure because while the single-crystal structure has the wrong chirality, all the atomic level values are comparable. Root-mean-square deviation (rmsd) values were good and yielded 0.02 Å for bond lengths, 0.82° for bond angles, and 2.15° for dihedral angles (only non-hydrogen atoms were considered for rmsd values). The quality of the internal structure of the simulations can also be analyzed by looking at the hydrogen bonds present in the system. EZT contains two hydrogen bonds, and Table 3 shows the heavy atom distances and angles for the single-crystal experimental structure and the

Table 3. Two O−H···O Bonds Present in EZT Heavy Atom Distances and Angles for the Experimental Structure (CSD Structure QUWYIR01[25]) and the Fully Optimized Structure

hydrogen bond	O···O (Exp.) (Å)	O···O (Comp.) (Å)	O−H···O (Exp.) (deg)	O−H···O (Comp.) (deg)
O3−H3···O1	2.775	2.662	155.0	171.4
O1−H1···O2	2.743	2.670	143.0	146.8

fully optimized simulations. As listed in Table 4, the largest error in the fully optimized ss-DFT structure of EZT-MH was

Table 4. Unit Cell Dimensions (Å) of EZT-MH from the Experiment (CSD Structure QATNEF01[23]), after Ss-DFT Optimization, and the Percent Error between the Two

lattice parameter	experimental	calculated	percent error (%)
a	6.2411	6.13980	−1.62
b	15.4844	15.40386	−0.52
c	22.3655	22.21187	−0.69
volume (Å3)	2161.3950	2100.72445	−2.81

−1.62% on the *a*-axis, with the average absolute error in the calculated unit cell dimensions being 0.94%. Rmsd assessment of the molecular structures revealed very good agreement with the experiment, yielding 0.02 Å for bond lengths, 0.44° for bond angles, and 2.06° for dihedral angles (considering only non-hydrogen atoms). EZT-MH has four O−H···O hydrogen bonds, and Table 5 lists these along with their heavy atom

Table 5. Four O−H···O Bonds Present in EZT-MH Heavy Atom Distances and Angles for the Experimental Structure (CSD Structure QATNEF01[23]) and the Fully Optimized Structure

hydrogen bond	O···O (Exp.) (Å)	O···O (Comp.) (Å)	O−H···O (Exp.) (deg)	O−H···O (Comp.) (deg)
O3−H3···O4	2.795	2.726	164.4	168.2
O4−H4···O1	2.745	2.677	174.2	174.9
O4−H5···O2	2.693	2.657	161.4	160.0
O1−H1···O4	2.701	2.659	167.7	173.3

distances and angles. The hydrogen bonds present in EZT-MH were on an average slightly shorter and closer to linear than those present in EZT. As with the fully optimized structures, the molecules of the fixed-lattice simulations were also evaluated using rmsd values. No significant differences were found between the two types of simulations, indicating that temperature-dependent unit cell changes have a negligible influence on the intramolecular structure of ezetimibe. This emphasizes that the structural differences between the fully optimized (0 K) and fixed-lattice (room temperature) simulations are intermolecular in nature, a finding that is
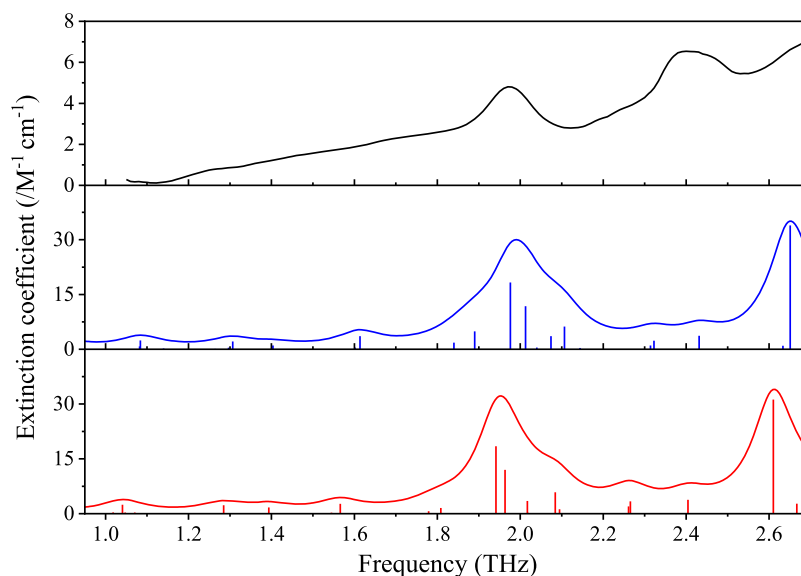
Figure 7. Experimental THz spectrum for EZT (top, black), the ss-DFT fully optimized simulation (middle, blue), and the ss-DFT fixed-lattice simulation (bottom, red).
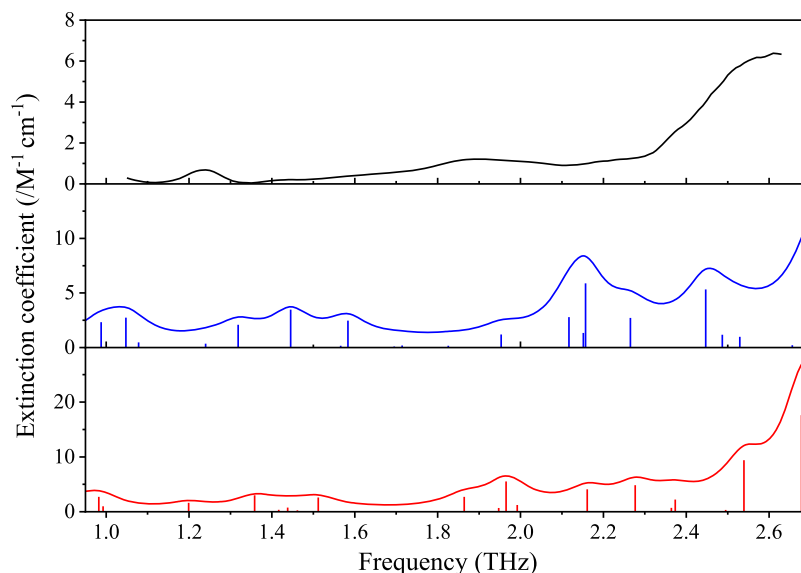

Figure 8. Experimental THz spectrum for EZT-MH (top, black), the ss-DFT fully optimized simulation (middle, blue), and the ss-DFT fixed-lattice simulation (bottom, red).

relevant to the interpretation of the THz spectra of these solids.

Simulated Terahertz Vibrational Spectra. Vibrational frequency analyses of the EZT and EZT-MH crystals yielded no negative vibrational modes, demonstrating that both ss-DFT fully optimized and fixed-lattice structures were energetic minima on their respective potential energy surfaces. Figure 7 shows the experimental THz vibrational spectrum along with the ss-DFT simulated spectra for the fully optimized and the fixed-lattice structures of EZT. The simulations produced very similar results and provided a good match with the experimental spectrum. In the fully optimized structure simulation (Figure 7 middle, blue), some peaks shifted to slightly higher frequencies, as expected from the reduced unit cell volume of a 0 K simulation. The experimental feature at 1.98 THz was reproduced as two major peaks at 1.98 and 2.01 THz in the simulated spectrum. The experimental peak at 2.42

THz was found to have shifted higher in the simulation at 2.65 THz. Comparing the fixed-lattice and fully optimized simulations (Figure 7 bottom, red) shows that the frequencies derived from the fixed-lattice structure were shifted to slightly lower energies, with the 1.98, 2.01, and 2.65 THz modes moving to 1.94, 1.96, and 2.61 THz, respectively.

The experimental spectrum and the ss-DFT simulated spectra for the fully optimized and the fixed-lattice structures of EZT-MH are shown in Figure 8. Unlike in Figure 7, these spectra were significantly different. Most of these differences were observed in the frequency positions of the predicted features, but there were also some changes in the calculated intensities for the lattice vibrations. In the fully optimized simulation (Figure 8 middle, blue), the experimental features at 1.24 and 1.88 THz were reproduced in the simulation slightly higher at 1.45 and 2.16 THz, respectively. The peak at the end of the experimental spectrum (2.6 THz) was

reproduced in the simulation at 2.84 THz. In the fixed-lattice simulation (Figure 8 bottom, red), the experimental features at 1.24 and 1.88 THz were reproduced in the simulation slightly higher at 1.36 and 1.97 THz, respectively. The peak at the end of the experimental spectrum (2.6 THz) was reproduced in the simulation as either a lower feature at 2.54 THz or a higher, more intense feature at 2.68 THz. Also, the strong feature seen in the fully optimized simulation at 1.05 THz shifted lower in the fixed-lattice simulation to 0.98 THz. Table 6 lists the

Table 6. Five Most Intense Peaks in the EZT and EZT-MH Fully Optimized Simulated Spectra between 1.0 and 2.8 THz and 1.0 and 2.62 THz, Respectively, along with Their Frequency in the Fixed-Lattice Simulations and the General Motion Type

fully optimized frequency (THz)	fixed-lattice frequency (THz)	mode type
	EZT	
1.98	1.94	torsion
2.01	1.96	rotation
2.11	2.08	torsion
2.65	2.61	torsion
2.80	2.75	torsion
	EZT-MH	
1.05	0.98	rotation
1.45	1.36	rotation
2.12	1.95	rotation
2.16	1.97	torsion
2.45	2.28	rotation

frequency positions of the five most intense peaks in the fully optimized simulations of EZT and EZT-MH with where these peaks shift in the fixed-lattice simulation. In the EZT simulations, there was a minimal shift between 0.03 and 0.05 THz. However in EZT-MH, there was much more dramatic shifting (between 0.07 and 0.19 THz) along with changes in the intensity distribution. ss-DFT also allows for the assignment of vibrational modes to specific motions, and the general mode types are provided in Table 6. The differences between the fully optimized and the fixed-lattice spectral simulations may come from anharmonicity in the potential energy surfaces that govern the frequency positions of the peaks. The calculations yield harmonic frequencies, but the changes in the lattice dimensions between 0 K and room temperature are driven by anharmonic factors that are at least partially captured in these comparative simulations. This is indicated by comparing the volumes of the fixed-lattice (room temperature) and full-optimized (0 K) unit cells, where EZT shows a unit cell contraction of 1.53%, but EZT-MH contracts by 2.8% over the same temperature range, suggesting that EZT has lesser anharmonic character, whereas EZT-MH has significantly more. Given the differences in the unit cell dimension changes, the anhydrous EZT peaks only slightly shifted between the fixed and full structural optimizations, whereas the EZT-MH spectral peaks moved considerably.

Analysis of the Energy Factors in Ezetimibe Crystals. The very good simulations of the structures and THz spectra of these solids indicate that the simulations accurately modeled the internal and external forces present in crystalline EZT and EZT-MH. This accuracy allows for a reliable evaluation of the intramolecular and intermolecular energies involved in these solid-state materials. One energetic factor that can be

compared between EZT and EZT-MH is the conformational energy of the ezetimibe molecule. The conformational energy of the ezetimibe molecule within EZT-MH was lower in energy than that in EZT by 5.47 kJ/mol (within the fully optimized structures). This was very similar to the value found in the fixed-lattice structures, 5.62 kJ/mol. The conformational difference between the ezetimibe molecules in the anhydrous and hydrated solids could be one factor in why EZT-MH is able to form over the parent species (water and ezetimibe). Cohesive energy is another important factor in the stability of solids. To make the cohesion comparable between the different EZT crystals, the cohesive energy per atom in the unit cell was calculated. EZT-MH had a greater cohesion magnitude of −6.18 kJ/mol than anhydrous EZT with −4.77 kJ/mol. These results show that the EZT-MH solid has both preferred intramolecular and intermolecular interaction energies.

To more fully understand the stability of EZT-MH, its Gibbs free energy can be compared to that of its individual parent species (ezetimibe and water). From the frequency analyses of EZT and EZT-MH, temperature-dependent Gibbs free-energy curves can be calculated. Along with Gibbs free-energy curves for EZT and EZT-MH, a Gibbs free-energy curve can be calculated for an isolated water molecule to model the free energy of a gas-phase molecule as would be released from a dehydrating solid. This can then be used to compare the free energies between EZT-MH and a linear combination of the Gibbs free energies of EZT and water (referred to as EZT + H_2O). Figure 9 illustrates the Gibbs free-energy curves based
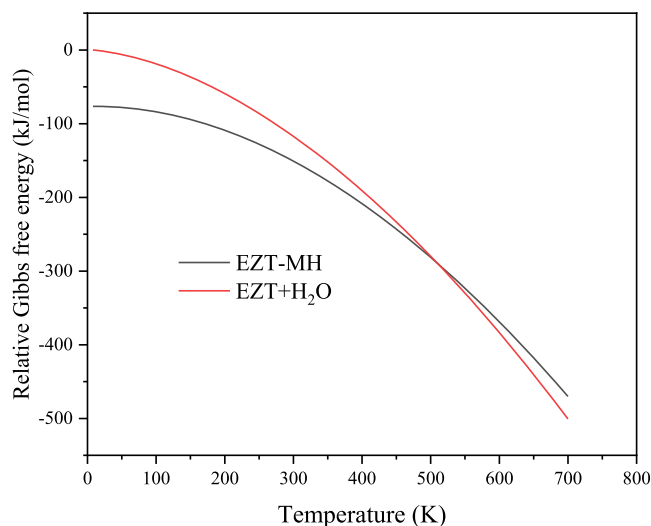
Figure 9. Relative Gibbs free-energy curve for EZT + H_2O (red) and EZT-MH (black). All energies are given as per crystallographic asymmetric unit (1 EZT, 1 H_2O). For clarity, the energy values have been set relative to a common zero.

on the fully optimized structures of EZT-MH and EZT, specifically including the EZT + H_2O result. EZT-MH was lower in energy (more stable) until the curves crossed at 509 K, well above the melting point of EZT (164 °C).[38] To note the relevant temperature points, EZT-MH was lower in energy than a combination of its parent species at 0 K (−76.78 kJ/mol) and 298 K (−34.13 kJ/mol). The same Gibbs free-energy analysis was applied to the fixed-lattice calculations, but little change was found, with the energy ranking preserved, and the curve crossing point modestly increased to 528 K. It should be mentioned that these energy calculations do not take into

account vibrational anharmonicity, which we have identified as being important to the EZT-MH system; however, this is unlikely to alter the energy rankings in the temperature range of most interest.

CONCLUSIONS

In this work, the powerful combination of THz spectroscopy and ss-DFT allowed for the analysis of the EZT and EZT-MH, which have similar crystalline morphologies and belong to the same space group. The good agreement between the simulations of the structures and THz spectra of these solids indicated that the simulations accurately modeled the internal and external forces present in crystalline EZT and EZT-MH. It was also discovered that the EZT-MH lattice vibrations exhibited greater anharmonic character than anhydrous EZT, which may be related to the greater number of hydrogen bonds in the hydrated sample. Using a THz spectrometer based on is-TPG with a humidity-controlled sample chamber, the hydration of ezetimibe in formulation tablets could be monitored in real time. The effect of excipients in the formulation was also successfully observed, showing that the rate of the solid-state transition of APIs was delayed in comparison with samples without excipients. These results indicate that the combination of THz-FDS experiments and ss-DFT simulations could be a very useful tool for monitoring and analyzing the solid-state transitions of in situ APIs and for quality control of solid formulations in pharmaceutical manufacturing.

ASSOCIATED CONTENT

ⓈI Supporting Information

The Supporting Information is available free of charge at https://pubs.acs.org/doi/10.1021/acs.jpca.2c00301.

PXRD pattern of EZT-MH (PDF)

AUTHOR INFORMATION

Corresponding Author

　Mizuki Mohara − *Hitachi High-Tech Corp., Hitachinaka 312-8504, Japan;* ⓞ orcid.org/0000-0003-4592-8446; Email: mizuki.oku.rr@hitachi-hightech.com

Authors

　Margaret P. Davis − *Department of Chemistry, Syracuse University, Syracuse, New York 13244, United States*
　Timothy M. Korter − *Department of Chemistry, Syracuse University, Syracuse, New York 13244, United States*
　Kei Shimura − *Hitachi High-Tech Corp., Hitachinaka 312-8504, Japan;* ⓞ orcid.org/0000-0001-8986-1090
　Touya Ono − *Hitachi High-Tech Corp., Hitachinaka 312-8504, Japan*
　Kenji Aiko − *Hitachi High-Tech Corp., Hitachinaka 312-8504, Japan*

Complete contact information is available at:
https://pubs.acs.org/10.1021/acs.jpca.2c00301

Notes
The authors declare no competing financial interest.

ACKNOWLEDGMENTS

REFERENCES

(1) Threlfall, T. L. Analysis of organic polymorphs. A review. *Analyst* **1995**, *120*, 2435−2460.

(2) Morris, K. R.; Griesser, U. J.; Eckhardt, C. J.; Stowell, J. G. Theoretical Approaches to Physical Transformations of Active Pharmaceutical Ingredients during Manufacturing Processes. *Adv. Drug Delivery Rev.* **2001**, *48*, 91−114.

(3) Krzyzaniak, J. F.; Williams, G. R.; Ni, N. Identification of Phase Boundaries in Anhydrate/Hydrate Systems. *J. Pharm. Sci.* **2007**, *96*, 1270−1281.

(4) Sanii, R.; Patyk-Kaźmierczak, E.; Hua, C.; Darwish, S.; Pham, T.; Forrest, K. A.; Zaworotko, M. J.; Zaworotko, M. Toward an Understanding of the Propensity for Crystalline Hydrate Formation by Molecular Compounds. Part 2. *Cryst. Growth Des.* **2021**, *21*, 4927.

(5) Pudipeddi, M.; Serajuddin, A. T. M. Trends in Solubility of Polymorphs. *J. Pharm. Sci.* **2005**, *94*, 929.

(6) Airaksinen, S.; Karjalainen, M.; Kivikero, N.; Westermarck, S.; Shevchenko, A.; Rantanen, J.; Yliruusi, J. Excipient Selection Can Significantly Affect Solid-State Phase Transformation in Formula Wet Granulation. *AAPS PharmSciTech* **2005**, *6*, No. E311.

(7) Miroshnyk, I.; Khriachtchev, L.; Mirza, S.; Rantanen, J.; Heinämäki, J.; Yliruusi, J. Insight into Thermally Induced Phase Transformations of Erythromycin A Dihydrate. *Cryst. Growth Des.* **2005**, *6*, 369−374.

(8) Fujii, K.; Aoki, M.; Uekusa, H. Solid-State Hydration/ Dehydration of Erythromycin A Investigated by Ab Initio Powder X-Ray Diffraction Analysis: Stoichiometric and Nonstoichiometric Dehydrated Hydrate. *Cryst. Growth Des.* **2013**, *13*, 2060−2066.

(9) Kim, Y.-s.; Rousseau, R. W. Characterization and Solid-State Transformations of the Pseudopolymorphic Forms of Sodium Naproxen. *Cryst. Growth Des.* **2004**, *4*, 1211−1216.

(10) Amado, A. M.; Nolasco, M. M.; Ribeiro-Claro, P. J. A. Probing Pseudopolymorphic Transitions in Pharmaceutical Solids Using Raman Spectroscopy: Hydration and Dehydration of Theophylline. *J. Pharm. Sci.* **2007**, *96*, 1366.

(11) Paiva, E. M.; Li, Q.; Zaczek, A. J.; Rohwedder, J. J. R.; Zeitler, J. A.; Axel Zeitler, J. Understanding the Metastability of Theophylline FIII by Means of Low-Frequency Vibrational Spectroscopy. *Mol. Pharm.* **2021**, *18*, 3578−3587.

(12) King, M. D.; Davis, E. A.; Smith, T. M.; Korter, T. M. Importance of Accurate Spectral Simulations for the Analysis of Terahertz Spectra: Citric Acid Anhydrate and Monohydrate. *J. Phys. Chem. A* **2011**, *115*, 11039−11044.

(13) Zeitler, J.; Kogermann, K.; Rantanen, J.; Rades, T.; Taday, P.; Pepper, M.; Aaltonen, J.; Strachan, C. Drug Hydrate Systems and Dehydration Processes Studied by Terahertz Pulsed Spectroscopy. *Int. J. Pharm.* **2007**, *334*, 78−84.

(14) Kogermann, K.; Zeitler, J. A.; Rantanen, J.; Rades, T.; Taday, P. F.; Pepper, M.; Heinämäki, J.; Strachan, C. J. Investigating Dehydration from Compacts Using Terahertz Pulsed, Raman, and near-Infrared Spectroscopy. *Appl. Spectrosc.* **2007**, *61*, 1265.

(15) King, M. D.; Korter, T. M. Effect of Waters of Crystallization on Terahertz Spectra: Anhydrous Oxalic Acid and Its Dihydrate. *J. Phys. Chem. A* **2010**, *114*, 7127−7138.

(16) Kawase, K.; Shikata, J.-i.; Imai, K.; Ito, H. Transform-Limited, Narrow-Linewidth, Terahertz-Wave Parametric Generator. *Appl. Phys. Lett.* **2001**, *78*, 2819−2821.

(17) Murate, K.; Taira, Y.; Tripathi, S. R.; Hayashi, S. i.; Nawata, K.; Minamide, H.; Kawase, K. A High Dynamic Range and Spectrally Flat Terahertz Spectrometer Based on Optical Parametric Processes in LiNbO3. *IEEE Trans. Terahertz Sci. Technol* **2014**, *4*, 523−526.

(18) Murate, K.; Kawase, K. Perspective: Terahertz Wave Parametric Generator and Its Applications. *J. Appl. Phys.* **2018**, *124*, 160901.

(19) Mohara, M.; Shimura, K.; Aiko, K.; Kawase, K. Terahertz Spectroscopy Using an Injection-Seeded Terahertz Parametric Generator for Quantitative Analysis and Inspection of over-the-

Counter Medicine Tablets. In *Proceedings of SPIE—The International Society for Optical Engineering*; Sadwick, L. P., Yang, T., Eds.; SPIE, 2018; Vol. *10531*, p 75.

(20) Lindenberg, M.; Kopp, S.; Dressman, J. B. Classification of Orally Administered Drugs on the World Health Organization Model List of Essential Medicines According to the Biopharmaceutics Classification System. *Eur. J. Pharm. Biopharm.* **2004**, *58*, 265.

(21) Farias, M. A. d. S.; Soares, F. L. F.; Carneiro, R. L. Crystalline Phase Transition of Ezetimibe in Final Product, after Packing, Promoted by the Humidity of Excipients: Monitoring and Quantification by Raman Spectroscopy. *J. Pharm. Biomed. Anal.* **2016**, *121*, 209−214.

(22) Brüning, J.; Alig, E.; Schmidt, M. U. Ezetimibe Anhydrate, Determined from Laboratory Powder Diffraction Data. *Acta Crystallogr., Sect. C: Cryst. Struct. Commun.* **2010**, *66*, o341.

(23) Śnieżek, M.; Stecko, S.; Panfil, I.; Furman, B.; Chmielewski, M. Total Synthesis of Ezetimibe, a Cholesterol Absorption Inhibitor. *J. Org. Chem.* **2013**, *78*, 7048.

(24) Sugandha, K.; Kaity, S.; Mukherjee, S.; Isaac, J.; Ghosh, A. Solubility Enhancement of Ezetimibe by a Cocrystal Engineering Technique. *Cryst. Growth Des.* **2014**, *14*, 4475−4486.

(25) Shimpi, M. R.; Childs, S. L.; Boström, D.; Velaga, S. P. New Cocrystals of Ezetimibe with L-Proline and Imidazole. *CrystEngComm* **2014**, *16*, 8984.

(26) Baron, P.; Mendrok, J.; Kasai, Y.; Ochiai, S.; Seta, T.; Sagi, K.; Suzuki, K.; Sagawa, H.; Urban, J. AMATERASU: Model for Atmospheric TeraHertz Radiation Analysis and Simulation. *J. Natl. Inst. Inf. Commun. Technol.* **2008**, *55*, 109−121.

(27) Hoshina, H.; Seta, T.; Iwamoto, T.; Hosako, I.; Otani, C.; Kasai, Y. Precise Measurement of Pressure Broadening Parameters for Water Vapor with a Terahertz Time-Domain Spectrometer. *J. Quant. Spectrosc. Radiat. Transfer* **2008**, *109*, 2303.

(28) Dovesi, R.; Erba, A.; Orlando, R.; Zicovich-Wilson, C. M.; Civalleri, B.; Maschio, L.; Rérat, M.; Casassa, S.; Baima, J.; Salustro, S.; et al. Quantum-Mechanical Condensed Matter Simulations with CRYSTAL. *Wiley Interdiscip. Rev.: Comput. Mol. Sci.* **2018**, *8*, No. e1360.

(29) Schäfer, A.; Horn, H.; Ahlrichs, R. Fully Optimized Contracted Gaussian Basis Sets for Atoms Li to Kr. *J. Chem. Phys.* **1992**, *97*, 2571.

(30) Perdew, J. P.; Burke, K.; Ernzerhof, M. Erratum: Generalized Gradient Approximation Made Simple (Physical Review Letters (1996) 77 (3865)). *Phys. Rev. Lett.* **1997**, *78*, 1396.

(31) Grimme, S.; Antony, J.; Ehrlich, S.; Krieg, H. A Consistent and Accurate Ab Initio Parametrization of Density Functional Dispersion Correction (DFT-D) for the 94 Elements H-Pu. *J. Chem. Phys.* **2010**, *132*, 154104.

(32) Grimme, S.; Ehrlich, S.; Goerigk, L. Effect of the Damping Function in Dispersion Corrected Density Functional Theory. *J. Comput. Chem.* **2011**, *32*, 1456−1465.

(33) Grimme, S.; Hansen, A.; Brandenburg, J. G.; Bannwarth, C. Dispersion-Corrected Mean-Field Electronic Structure Methods. *Chem. Rev.* **2016**, *116*, 5105.

(34) Donà, L.; Brandenburg, J. G.; Bush, I. J.; Civalleri, B. Cost-Effective Composite Methods for Large-Scale Solid-State Calculations. *Faraday Discuss.* **2020**, *224*, 292.

(35) Groom, C. R.; Bruno, I. J.; Lightfoot, M. P.; Ward, S. C. The Cambridge Structural Database. *Acta Crystallogr., Sect. B: Struct. Sci., Cryst. Eng. Mater.* **2016**, *72*, 171−179.

(36) Pascale, F.; Zicovich-Wilson, C. M.; López Gejo, F.; Civalleri, B.; Orlando, R.; Dovesi, R. The Calculation of the Vibrational Frequencies of Crystalline Compounds and Its Implementation in the CRYSTAL Code. *J. Comput. Chem.* **2004**, *25*, 888−897.

(37) Noel, Y.; Zicovich-Wilson, C. M.; Civalleri, B.; D'Arco, P.; Dovesi, R. Polarization Properties of ZnO and BeO: An Ab Initio Study through the Berry Phase and Wannier Functions Approaches. *Phys. Rev. B: Condens. Matter Mater. Phys.* **2002**, *65*, 014111.

(38) Ezetimibe. The Merck Index Online 15th Edition, Monograph ID: M5228. https://www.rsc.org/Merck-Index/monograph/m5228/ezetimibe?q=unauthorize (accessed Dec 12, 2021).